Apparent size and morphology of bacterial microcompartments varies with technique

Nolan W. Kennedy[1], Jasmine M. Hershewe[2,3], Taylor M. Nichols[2], Eric W. Roth[4], Charlene D. Wilke[4], Michael C. Jewett[2,3,5,6,7], Danielle Tullman-Ercek[2,7*]

[1] Interdisciplinary Biological Sciences Graduate Program, Northwestern University, Evanston, Illinois, United States of America

[2] Department of Chemical and Biological Engineering, Northwestern University, Evanston, Illinois, United States of America

[3] Chemistry of Life Processes Institute, Evanston, Illinois, United States of America

[4] Northwestern University Atomic and Nanoscale Characterization Experimentation Center, Northwestern University, Evanston, Illinois, United States of America

[5] Robert H. Lurie Comprehensive Cancer Center, Northwestern University, Chicago, Illinois, United States of America

[6] Simpson Querrey Institute, Northwestern University, Chicago, Illinois, United States of America

[7] Center for Synthetic Biology, Northwestern University, Evanston, Illinois, United States of America

* Corresponding author

E-mail: ercek@northwestern.edu (DTE)

Abstract

Bacterial microcompartments (MCPs) are protein-based organelles which encapsulate metabolic pathways. Metabolic engineers have recently sought to repurpose MCPs to encapsulate heterologous pathways to increase flux through pathways of interest. As MCP engineering becomes more common, standardized methods for analyzing changes to MCPs and interpreting results across studies will become increasingly important. In this study, we demonstrate that different imaging techniques yield variations in the apparent size of purified MCPs from *Salmonella enterica* serovar Typhimurium LT2, likely due to variations in sample preparation methods. We provide guidelines for preparing samples for MCP imaging and outline expected variations in apparent size and morphology between methods. With this report we aim to establish an aid for comparing results across studies.

Introduction

Scientific research has recently come under fire for what is being dubbed a crisis of reproducibility. Current studies estimate that 75-90% of findings in high-profile journals are not reproducible [1]. The issue has seeped into fields across every domain of scientific inquiry [2]. While the cause of any given irreproducible result will vary from case to case, a lack of technique standardization across studies can lead to artefactual results or false conclusions [3]. In fields in which different techniques are employed to test similar hypotheses, it is important to place results into the proper context and understand the limitations of each technique. Here, we provide guidelines for technique standardization and result interpretation in the bacterial microcompartment engineering field.

Bacterial microcompartments (MCPs) are protein-based organelles found in diverse species of bacteria [4–6]. These were originally identified in cyanobacteria and were hypothesized to be viruses based on their appearance [7,8]. However, these structures were later determined to be important for the carbon concentrating mechanism for certain species of autotrophic microbes [9–12]. Since then, numerous diverse types of MCPs have been identified in species ranging from cyanobacteria and halophilic ocean-dwelling bacteria, to enteric pathogens and soil-dwelling microbes [13,14]. In addition to the cyanobacterial compartments used for carbon fixation, many MCPs are used by enteric pathogens for the metabolism of unique carbon sources that move through toxic or volatile intermediates, imparting a competitive advantage [15–18].

The flagship archetype for metabolic MCPs is the 1,2-propanediol utilization (Pdu) MCP found in *Salmonella enterica.* The Pdu MCP encapsulates the enzymatic machinery necessary for metabolism of 1,2-propanediol (1,2-PD), a carbon source found in the gut of *Salmonella* hosts [15]. The 1,2-PD metabolic enzymes are surrounded by a protein shell composed of multiple types of trimeric, pentameric, and hexameric shell proteins. The reported size of these irregularly-shaped protein organelles varies widely from 77-220 nm in diameter (**S1 Table**), and rigorous methods for size quantification are sparse [8,13,15,19–23].

The Pdu MCP has been studied in-depth since the early 1990s, but it has recently increased in popularity due to its potential utility in metabolic engineering [24–26]. Metabolic engineers have sought to increase flux through target pathways of interest by increasing local concentrations of enzymes and their substrates [27]. MCPs can accomplish this task and offer the potential added benefit of sequestering toxic or volatile intermediates from damaging or escaping the cell [28,29]. They also have the potential to reduce unwanted side reactions and provide private cofactor pools separate from central metabolism [30].

Recent efforts to engineer MCPs focused on loading heterologous proteins to the lumen of these structures, as well as modifying the MCP shell to alter substrate and product diffusion [23,31]. Even modest engineering efforts can affect the size, shape, and morphology of MCPs. For example, knocking out or over-expressing different shell proteins leads to dramatic changes in the shape of MCPs, with many appearing to be long, hollow tubes [32–36]. As engineering efforts continue, it will become increasingly important to have a standardized set of tools for the field to determine and compare the size, shape, and morphology of engineered or altered MCPs across different studies. To date, there is no widely agreed-upon method for visualizing and measuring MCPs, with labs across the field utilizing their own preferred technique. Here we demonstrate that different techniques can yield variable apparent results, even on identical samples. We provide an outline for choosing an appropriate technique and subsequently correlate the results across the many visualization and sizing techniques used in the field.

Methods

Microcompartment Expression and Purification

Intact Pdu MCPs were purified from lysed cultures of *Salmonella enterica* serovar Typhimurium LT2 using a centrifugation process as previously described [37–39]. Briefly, starter cultures were grown in 5 mL of LB-Miller for 24 hours at 30°C, 225 RPM and subsequently subcultured 1:1000 into 200 mL of no carbon-E (NCE) minimal media (29 mM KH_2PO_4, 34 mM K_2HPO_4, 17 mM $Na(NH_4)HPO_4$, 1 mM $MgSO_4$, and 50 µM ferric citrate) supplemented with 42 mM succinate as a carbon source and 55 mM 1,2-propanediol for MCP induction. NCE cultures were grown at 37°C, 225 RPM to a final target OD_{600} of ~1-1.5, after which they were harvested and lysed. The lysed cultures were centrifuged at 12,000 x G for 5 minutes to remove cell debris. MCPs were then pelleted from the resulting supernatant through centrifugation at 21,000 x G for

20 minutes and collected. The total protein concentration of MCP samples was measured using the Pierce^{TM} BCA Protein Assay Kit (Thermo Scientific) per the manufacturer's instructions, and concentrations were normalized as necessary for each analysis method. All MCP samples were stored at 4°C until use and were prepared for analysis within 5 days of purification to avoid MCP aggregation and degradation [40].

Protein Electrophoresis

Purified MCPs were assessed for composition by SDS-PAGE as previously described [38]. Briefly, MCP samples were boiled in Laemmli buffer at 95°C for 5-7 minutes. The denatured samples were then loaded onto 15% SDS-PAGE gels and separated at 120 V for 90 minutes. Approximately 2-2.25 μg total protein was loaded for each sample, as measured by BCA assay. Gels were then stained with Coomassie and imaged using the Bio-Rad ChemiDoc XRS+ (**S1 Fig**).

Negative-Stain Transmission Electron Microscopy

Samples were set on 400 mesh Formvar-coated copper grids (EMS Cat# FF400-Cu) with a carbon film. Grids were treated by glow discharge using a PELCO easiGlow glow discharge cleaning system for a total of 10 seconds at 15 mA. MCP samples were placed onto the grids immediately following glow discharge. We found that staining and contrast were best if MCPs were left undiluted (between 0.5-1.0 mg/mL). A volume of 10 μL of purified MCPs was pipetted onto the surface of the grids, which were held in place by negative-action tweezers. The samples were allowed to sit for 2 minutes before being wicked away with filter paper. Note that some of the liquid should always be left on the grid to avoid sample collapse. The samples were washed three times by dipping the grid in a small droplet of deionized water for three seconds. The samples were fixed by placing 10 μL of 2% (v/v) glutaraldehyde onto the grid for 2 minutes. Note that glutaraldehyde should be stored under N_2, and the 2% dilution should be made fresh before each sample preparation session. After the 2-minute incubation, the glutaraldehyde was wicked away using filter paper and the sample was washed three times in deionized water. Samples were stained with 1% (w/v) aqueous uranyl acetate (UA) by applying 10 µL of UA to the grids for 2 minutes. The UA was wicked away completely using filter paper. Note that all samples, fixative, stain, and deionized water were spun at 12,000 x G for 2 minutes before use to remove any aggregates. Samples were imaged at the Northwestern Electron Probe Instrumentation Center (EPIC) using the Hitachi HT-7700 Biological S/TEM Microscope and the Galtan Orius 4k x 2.67k digital camera.

For samples that were exchanged into solvent to prevent collapsing, samples were first fixed as described above in 2% glutaraldehyde. The samples were exchanged into 30% (v/v) ethanol for 1 minute, then 50% (v/v), 70% (v/v), and 90% (v/v) ethanol, followed by 100% ethanol three times. After this exchange into ethanol, samples were exchanged into 50% (v/v) and then 100% hexamethyldisilazane (HMDS). Samples exchanged into 100% HMDS were stained with UA as described above.

Scanning Electron Microscopy

Samples were spotted and fixed onto 400 mesh Formvar-coated copper grids (EMS Cat# FF400-Cu) and processed through a 100% ethanol exchange as described above. Grids were placed into a sample holder and loaded into a Tousimis critical point dryer. The critical point dryer was run for a 10-minute purge cycle. Grids were mounted onto SEM stubs with carbon tape and coated with 6 nm of gold/palladium in a Cressington 208H sputter coater. Grids were imaged using a Hitachi SEM with 2 kV accelerating voltage and a 4 mm working distance.

Cryo Transmission Electron Microscopy

Lacey Carbon 200 mesh Cu grids (EMS Cat# LC200-CU) were glow discharged in a Pelco easiGlow glow discharger for 30 seconds at 30 mA. 4 µL of sample solution was carefully pipetted onto the grids and plunge frozen in liquid ethane in a FEI Vitrobot Mark III with a blotting time of 5 seconds and blot offset of 0.5 mm. Grids were stored in liquid nitrogen and loaded into a Gatan 626.6 Cryo Transfer Holder cooled down to -170°C prior to observation in a JEOL JEM-1230 LaB6 emission TEM running at 100 kV. Images were collected with a Gatan Orius SC1000 CCD Camera, Model 831.

Transmission Electron Microscopy of Ultra-thin Sections

Samples were pelleted at 21,000 x G in an Eppendorf 5424 microcentrifuge for 10 minutes. Pelleted samples were fixed with 2.5% (v/v) glutaraldehyde and 2% (v/v) paraformaldehyde in 0.1M PBS, post-fixed with 1% (w/v) OsO4 and 1% (w/v) UA, dehydrated in a graded series of ethanol, infiltrated with EMBed 812 epoxy resin, and embedded in beam capsules. The embedded samples were polymerized at 60°C for 48 hours prior to ultra-thin sectioning utilizing a Leica UC7 ultramicrotome. Sections were collected on 150 mesh Cu grids with a formvar/carbon membrane and stained with 3% (w/v) UA in 50% (v/v) methanol and Reynold's lead citrate to further enhance contrast. The samples were observed in a JEOL JEM-1230 LaB6 emission TEM at 100 kV. Images were collected with a Gatan Orius SC1000 CCD Camera, Model 831.

Dynamic Light Scattering Measurements

Samples were centrifuged at 12,000 x G for 5 minutes at 4°C immediately before dynamic light scattering (DLS) analysis to remove aggregated or insoluble protein. Dynamic light scattering was performed on a Zetasizer Nano ZS (Malvern Instruments Ltd., UK) with a measurement angle of 173°. Measurements were collected in triplicate at 4°C for 13 scans per measurement. Refractive index and temperature-adjusted viscosity were obtained from the instrument's parameter library.

Nanoparticle tracking analysis was performed on a Nanosight NS300 using a 488 nm (blue) laser (Malvern Instruments Ltd., UK). Instrument settings were adjusted according to manufacturer recommendations. Measurements were collected for a duration of 60 s in 5 runs using a 1 mL syringe and a syringe pump speed of 30. Measurements were collected at room temperature.

Image Analysis and Sizing

Images were contrast-adjusted and cropped using ImageJ [41]. For MCP sizing, images were scale-corrected based on the instrument used to collect the images. The oval tool was used to manually trace an ellipse surrounding MCPs. The longest diameter in the ellipse, corresponding to the widest diameter for the MCP, was recorded. Further data analysis was carried out using Microsoft Excel or R. Two-tailed t-tests were used to determine significance of differences between populations.

Results and Discussion

Negative-stain TEM of purified MCPs yields MCPs that appear deflated

Imaging MCPs using negative-stain transmission electron microscopy (TEM) is a standard technique used by the MCP field that has been widely adopted since Sinha and colleagues first described a method for MCP purification [39]. This technique enables clear identification of the border of each MCP, facilitating descriptions of shape and morphology (**Table 1**). Additionally, these results are generally higher contrast than techniques that involve imaging unpurified MCPs, such as TEM of ultra-thin cell sections.

Table 1. Comparison of different techniques used for MCP analysis.

Method	Strengths	Weaknesses	Specialized Equipment	Previous Works
Transmission Electron Microscopy (TEM)	•Relatively simple instrumentation, compared to other techniques •Sample preparation is fast and straightforward •Easy to see surface and shape morphology •History of use in the field	•Compartments appear collapsed due to sample preparation methods •Size analysis is slow compared to DLS, etc.	•Glow Discharge System •Transmission Electron Microscope	[20,22–24,30,32,37,40,42–52]
Ultra-thin section Transmission Election Microscopy (TEM)	•Can visualize compartments in native context (does not require purification) •History of use in the field	•Relatively slow and difficult sample preparation, requiring multiple pieces of specialized equipment •Cannot readily visualize surface morphology •*In vivo* images are difficult to analyze due to other cellular components •Due to the irregular shape of compartments, size determination using this method yields a wide distribution of apparent compartment diameters, skewing results	•Ultramicrotome •Transmission Electron Microscope	[8,15,16,19,22,24,30,33–36,40,42–45,51,53–55]
Scanning Electron Microscopy (SEM)	•Compartments appear more true-to-size (less collapsed) •Can visualize surface and shape morphology	•Compartments appear slightly collapsed •Staining with a metal coat can hide surface morphologies and alter apparent size •Sample preparation and imaging is relatively complex and requires multiple pieces of specialized equipment	•Glow Discharge System •Critical Point Dryer •Sputter Coater •Scanning Electron Microscope	
Transmission Electron Cryo-microscopy (Cryo TEM)	•Compartments retain solution size, shape, and morphology the best	•Sample preparation and imaging is difficult •Contrast is low due to lack of staining	•Glow Discharge System •Plunge freezer •Cryo transfer holder •Transmission electron microscope	[21,56]

Dynamic Light Scattering (DLS), etc.	•The most rapid, high-throughput method for determining the size distribution of a population of compartments	•Does not provide information on morphology	•DLS, Zeta Sizer, other system	[40,47,51]

Table 1 lists the various techniques, along with their strengths and weakness, that are utilized in the MCP field and are assessed in this work. We have also included a brief list of specialized equipment necessary for each technique, and a list of previous works in the MCP field in which each technique was used. Our hope is that this will enable selection of the technique best-suited for each study.

A drawback to the negative-stain TEM technique is that it requires sample dehydration as part of the sample preparation process. This ultimately leads to MCP collapse or deflation, as indicated in **Fig 1A**. Dark staining is present at the MCP interior, indicating that the stain is pooling in the collapsed, cup-shaped MCPs. To avoid this, fixing with glutaraldehyde is often used, but does not seem to completely prevent MCP collapse. MCPs appeared to be 102 ± 17 nm (mean ± standard deviation) in diameter when measured in images generated with this method (**Fig 2**).

Fig 1. TEM of purified MCPs. (A) Schematic representation and transmission electron micrograph of negatively stained purified MCPs. Note that MCPs appear collapsed as evidenced by the pooled stain near the center of MCPs. (B) Schematic representation and transmission electron micrograph of negatively stained purified MCPs which were first dehydrated in ethanol and a high vapor pressure solvent (HMDS). Note that MCPs appear less collapsed than in (A). Scale bar (white) is 100 nm.

Fig 2. Apparent size of MCPs analyzed with different imaging techniques. Box-and-whisker plot of the size distribution of MCPs analyzed with various techniques. Note that apparent size and distribution varies widely with each technique. The only populations which are not significantly different (as defined by a p-value greater than .001 in a two-tailed t-test) are TEM of purified MCPs vs thin section TEM and SEM of purified MCPs vs TEM of dehydrated samples ($p = .12$ and .26, respectively). $N = 300$ for all, where 100 measurements were made for each of three biological replicates (three different MCP growths and purifications). Abbreviations: transmission electron microscopy (TEM), transmission electron microscopy with samples dehydrated in hexamethyldisilazane (TEM + HMDS), scanning electron microscopy (SEM), cryo transmission electron microscopy (Cryo TEM), ultra-thin section transmission electron microscopy (UTS TEM).

We attempted a number of alterations to the standard sample preparation technique to reduce MCP collapse. This included critical point drying and sample buffer exchange from the aqueous sample buffer into a high vapor-pressure solvent. These methods improved MCP structure retention, especially in samples that were exchanged into the high vapor-pressure solvent hexamethyldisilazane (HMDS) (**Fig 1B**). Overall this sample preparation technique increased the average apparent diameter of the MCPs by 22% to 124 ± 17 nm and required minimal additional steps (less than an hour of additional preparation time, even with multiple samples) (**Fig 2**). However, the exchange into HMDS led to inconsistent staining across the sample grid. This is likely due to the minimal miscibility of HMDS and the aqueous UA stain. In spite of these inconsistencies, this technique may be useful when attempting to estimate the approximate diameter of engineered MCPs using negative-stain TEM.

Critical point drying and scanning electron microscopy reduces apparent MCP collapse

A technique that has not been widely adopted in the MCP field is scanning electron microscopy (SEM) (**Table 1**). This technique utilizes critical point drying to retain the structure of imaged samples. This is followed by treating with a sputter coater, which coats the sample in a thin layer of metal. In contrast to negative-stain TEM sample preparation, this method does not utilize an aqueous stain. For this reason, we hypothesized that critical point drying and SEM would lead to MCPs that appeared more inflated. Indeed, MCPs that were subjected to this sample preparation and imaging workflow did appear slightly more inflated than either of the negative-stain TEM methods described above (**Fig 3**). Coating for SEM also allows for tuning of the coat thickness, though there is an upper limit as increasing the metal coating thickness hindered detection of surface morphology (**Fig 3B, C**). For example, in **Fig 3B**, a coat thickness of >6 nm was used and occluded some morphological features visible in **Fig 3C**, which had a coat thickness of 6 nm. For this reason, we recommend using a minimal coat thickness (6 nm) **(Fig 3C)**, although finding a balance between optimal coat thickness, accelerating voltage, and scan speed will be necessary for each case. Overall, this technique yielded MCPs that appeared 24% (126 ± 17 nm diameter) larger, on average, than the standard negative-stain TEM method widely adopted by the field and allowed for visualization of MCP surface morphology comparable to the detail seen with negative-stain TEM (**Fig 2**). However, the additional sample preparation steps and specialized equipment may make this technique less appealing for many applications. Specifically, SEM sample preparation and imaging time per sample were approximately double that of TEM.

Fig 3. SEM of purified MCPs. (A) Schematic representation of MCPs imaged by SEM. (B) SEM of MCPs with >6 nm of gold staining. (C) SEM of MCPs with the minimal 6 nm gold coat thickness. Note that MCPs appear more inflated than in Figure 1A and surface features are apparent. Scale bars (white) are 100 nm.

Cryo transmission electron microscopy maintains inflated MCPs

Recently, cryogenic transmission electron microscopy (cryo TEM) was used to determine the structure of an intact MCP from *Haliangium ochraceum* [56]. This MCP is unique in that it is relatively small (6.5 MDa, as opposed to the 600 MDa Pdu MCP), and regular in shape [57]. We hypothesized that because cryo TEM keeps the sample in vitreous ice and does not remove the sample from its native buffer, it would be best suited for retaining fully-inflated MCPs in their native shape and diameter (**Fig 4**). Indeed, samples that were imaged using cryo TEM produced images that on average appeared the largest of any of the techniques we attempted (138 ± 21 nm diameter). These MCPs appeared 35% larger in diameter than the standard negative-stain TEM technique and 10% larger than SEM. Samples imaged using cryo TEM also had similar variation in size observed by the other techniques, indicating that the higher average size is not due to large outliers (**Fig 2**). Indeed, cryo TEM had the second fewest outliers of any of the imaging techniques we used to assess the population size distribution.

Fig 4. Cryo TEM of purified MCPs. (A) Schematic representation of cryo TEM of MCPs. Note that MCPs retain their native shape and are frozen in a layer of vitreous ice. (B) Micrographs of purified MCPs visualized using cryo TEM. Scale bars (white) are 100 nm.

While cryo TEM retained inflated MCPs, the lack of any contrast agent makes visualizing surface features nearly impossible. Additionally, the initial technical training for sample preparation and imaging using cryo TEM is challenging. However, an experienced microscopist can acquire cryo TEM data routinely in a single day. By contrast, chemical processing for TEM of ultra-thin sections can take several days and includes extra steps such as ultramicrotomy. Therefore, since this technique retains the native, uncollapsed state of MCPs, labs may choose to use this technique if a study is primarily focused on a change in MCP size or shape, especially on a limited number of samples (**Table 1**).

Ultra-thin section transmission electron microscopy yields large variation in apparent size

Besides negative-stain TEM of purified MCPs, the technique most widely used in the field is TEM of ultra-thin sections. This technique has been used both on purified MCPs as well as MCPs in cells. In the earliest studies in the field, this technique was the only available option for visualizing MCPs, as a purification method was not published until relatively recently (carboxysomes were discovered in 1956 but the method for Pdu MCP purification was not published until 2012) [7,39]. This allowed for visualization of MCPs within their native context and provided researchers with a means to determine if genetic manipulations altered the expression, size, shape, and cytoplasmic distribution of MCPs.

However, TEM of ultra-thin sections has a number of drawbacks that make it a suboptimal choice for many applications. Due to the irregular shape of Pdu MCPs, ultra-thin sections produce highly variable apparent diameters (99 ± 32 nm) depending on where the MCP is sectioned (**Fig 5**). Using this technique, we found the largest variation in apparent MCP diameter, with measurements both much larger and much smaller than all previous techniques (**Fig 5**). Indeed, MCPs appeared on average 28% smaller in diameter than with cryo TEM, and the variation was between 1.5 and 1.9 times greater than all other methods (**Fig 2**). Qualitatively, MCPs visualized using TEM of ultra-thin sections appeared more rounded and less angular than with other techniques. However, this is not always the case across the field, as other labs have used this technique to produce MCP images that appear to retain their native angularity [8].

Fig 5. TEM of ultra-thin sections of purified MCPs. (A) Schematic representation of an MCP undergoing ultra-thin sectioning. Note that due to the irregular shape of MCPs, thin sectioning will lead to a wide range of apparent diameters. (B) Micrographs of purified and ultra-thin sectioned MCPs. Scale bar (white) is 250 nm.

Additionally, preparation of ultra-thin sections is a challenging technique to master, and it can be difficult to determine the true boundaries of MCPs when they are visualized within cells. Due to these many drawbacks, we recommend only using TEM of ultra-thin sections when it is necessary to view MCPs in their native context in the cytoplasm or when it is necessary to image the interior of MCPs (**Table 1**).

Dynamic light scattering and nanoparticle tracking analysis enables higher-throughput MCP sizing

While microscopy allows researchers to visualize the morphology of MCPs, this may not be necessary for all studies. These imaging techniques are relatively low-throughput, and size determination is slow. One higher-throughput option for MCP sizing is particle sizing via dynamic light scattering (DLS). In this study we compared two different DLS-based techniques -- Nanosight for nanoparticle tracking analysis (NTA), and Zeta Sizer for population-based size measurements. Sizing analyses were performed on MCPs in solution (**Fig 6**), and particle size distributions (PSDs) were acquired (**Figs 6A and 6B**). When analyzed via Nanosight, the resulting distribution peak reached a maximum at 132 nm (**Fig 6A**). When analyzed via Zeta Sizer, the calculated distribution reached an intensity maximum of 122 nm (**Fig 6B**). Generally, the particle size distribution peak obtained via Nanosight was narrower than in the Zeta Sizer analysis. The average diameter measured by NTA was 149.5 ± 0.7 nm, which was larger than the 122.04 ± 0.5 nm measured by the Zeta Sizer (**Fig S2**). The disparity in mean diameter comes from large aggregates observed in the NTA experiment (**Fig S3**). To directly compare the sizing of Nanosight and Zeta Sizer, we consider differences between the mode diameter of Nanosight and the mean diameter (Z_{ave}) of the Zeta Sizer to be the most accurate comparison. The mode diameter of 130.7 ± 1.0 nm is slightly higher than the measured 122.04 ± 0.5 nm observed in Zeta Sizer measurements. Finally, the polydispersity index (PDI) calculated via Zeta Sizer was 0.045 ± 0.001, indicating that purified MCPs are monodisperse, as expected. We attribute discrepancies in diameter measurements to differences between the measurement techniques and their respective calculations of particle diameter. The full experiment report obtained for NTA measurements is shown in **S3 Fig.**

Fig 6. Higher-throughput sizing of purified MCPs using DLS. Sizing MCPs in solution via light scattering techniques. (A) Particle size distributions measured via Nanosight, and (B) Zeta Sizer.

To further assess the stability of DLS sizing measurements over an order of magnitude of concentrations of MCPs, we compared size measurements at 50 µg/mL and 500 µg/mL MCPs using Zeta Sizer (**S4 Fig**). Importantly, the raw correlation data obtained at 50 µg/mL and 500 µg/mL were in good agreement; the resulting Z_{ave} values calculated were 121.1 ± 0.32 nm and 122.0 ± 0.51 nm, respectively **(S4A and S4B Figs)**. Polydispersity indices obtained for MCPs at 50 µg/mL and 500 µg/mL were 0.069 ± 0.001 and 0.045 ± 0.001, respectively, indicating a high degree of uniformity of MCPs (**S4C Fig**). Full intensity, number, and volume PSDs for DLS measurements are presented in **S4D-F Figs.** As expected, we observed similar PSDs for measurements collected at 50 µg/mL and 500 µg/mL MCPs. Intensity PSDs displayed maximum intensities at ~122 nm. Number and volume PSDs displayed maxima near ~90 nm, and were left-shifted with respect to the intensity PSDs. Slight shifting of the PSDs between intensity, number, and volume distributions is most likely due to the non-spherical nature of MCPs. The consistency and stability of DLS measurements over an order of magnitude of concentration indicate that Zeta Sizer is a suitable technique for analysis of MCPs over a range of concentrations. Notably, the diameters obtained by Zeta Sizer appear more similar to the results obtained by SEM or TEM samples treated with HMDS but are 12-13% smaller than MCPs observed by cryo TEM. However, Nanosight results appeared most similar to those obtained by cryo TEM (132 nm vs. 138 nm).

Conclusion

Our results suggest that the technique used to visualize and measure MCPs can alter how we interpret our experimental results. This is especially important when comparing results across studies which used different techniques to assess their results. Our hope is that this study can provide a guideline for the appropriate use of each of the many available techniques used in the field to assess MCPs. Our results can also be used to contextualize and compare results across different studies by providing approximate percent changes in apparent size for each technique.

Acknowledgements

The authors would like to thank Robert Colby, Mark Heinnickel, and Giovanni Pilloni for their helpful thoughts on additional methods to include in this work, and members of the Tullman-Ercek lab for helpful comments during the preparation of this manuscript.

References

1. Begley CG, Ioannidis JPA. Reproducibility in Science: Improving the Standard for Basic and Preclinical Research. Circ Res. 2015 Jan 2;116(1):116–26.

2. Goodman SN, Fanelli D, Ioannidis JPA. What does research reproducibility mean? Sci Transl Med. 2016 Jun 1;8(341):341ps12-341ps12.

3. Allison DB, Brown AW, George BJ, Kaiser KA. Reproducibility: A tragedy of errors. Nature. 2016 Feb;530(7588):27–9.

4. Bobik TA, Lehman BP, Yeates TO. Bacterial microcompartments: widespread prokaryotic organelles for isolation and optimization of metabolic pathways. Mol Microbiol. 2015 Oct;98(2):193–207.

5. Held M, Quin MB, Schmidt-Dannert C. Eut Bacterial Microcompartments: Insights into Their Function, Structure, and Bioengineering Applications. J Mol Microbiol Biotechnol. 2013;23(4–5):308–20.

6. Rae BD, Long BM, Badger MR, Price GD. Functions, Compositions, and Evolution of the Two Types of Carboxysomes: Polyhedral Microcompartments That Facilitate CO2 Fixation in Cyanobacteria and Some Proteobacteria. Microbiol Mol Biol Rev. 2013 Sep 1;77(3):357–79.

7. Drews G, Niklowitz W. [Cytology of Cyanophycea. II. Centroplasm and granular inclusions of Phormidium uncinatum]. Arch Mikrobiol. 1956;24(2):147–62.

8. Shively JM, Decker GL, Greenawalt JW. Comparative Ultrastructure of the Thiobacilli. J Bacteriol. 1970 Feb;101(2):618–27.

9. Shively JM, Ball F, Brown DH, Saunders RE. Functional organelles in prokaryotes: polyhedral inclusions (carboxysomes) of Thiobacillus neapolitanus. Science. 1973 Nov 9;182(4112):584–6.

10. Dou Z, Heinhorst S, Williams EB, Murin CD, Shively JM, Cannon GC. CO $_2$ Fixation Kinetics of *Halothiobacillus neapolitanus* Mutant Carboxysomes Lacking Carbonic Anhydrase Suggest the Shell Acts as a Diffusional Barrier for CO $_2$. J Biol Chem. 2008 Apr 18;283(16):10377–84.

11. Price GD, Badger MR. Expression of Human Carbonic Anhydrase in the Cyanobacterium Synechococcus PCC7942 Creates a High CO2-Requiring Phenotype 1. Plant Physiol. 1989 Oct;91(2):505–13.

12. Mangan NM, Brenner MP. Systems analysis of the CO2 concentrating mechanism in cyanobacteria. eLife. 2014 Apr 29;3:e02043.

13. Chowdhury C, Sinha S, Chun S, Yeates TO, Bobik TA. Diverse Bacterial Microcompartment Organelles. Microbiol Mol Biol Rev MMBR. 2014 Sep;78(3):438–68.

14. Axen SD, Erbilgin O, Kerfeld CA. A Taxonomy of Bacterial Microcompartment Loci Constructed by a Novel Scoring Method. Tanaka MM, editor. PLoS Comput Biol. 2014 Oct 23;10(10):e1003898.

15. Bobik T, Havemann G, Busch R, Williams D, Aldrich H. The propanediol utilization (pdu) operon of Salmonella enterica serovar typhimurium LT2 includes genes necessary for formation of polyhedral organelles involved in coenzyme B-12-dependent 1,2-propanediol degradation. J Bacteriol. 1999 Oct;181(19):5967–75.

16. Brinsmade SR, Paldon T, Escalante-Semerena JC. Minimal Functions and Physiological Conditions Required for Growth of Salmonella enterica on Ethanolamine in the Absence of the Metabolosome. J Bacteriol. 2005 Nov 15;187(23):8039–46.

17. Chen P, Andersson DI, Roth JR. The control region of the pdu/cob regulon in Salmonella typhimurium. J Bacteriol. 1994 Sep;176(17):5474–82.

18. Stojiljkovic I, Bäumler AJ, Heffron F. Ethanolamine utilization in Salmonella typhimurium: nucleotide sequence, protein expression, and mutational analysis of the cchA cchB eutE eutJ eutG eutH gene cluster. J Bacteriol. 1995;177(5):1357–1366.

19. Parsons JB, Dinesh SD, Deery E, Leech HK, Brindley AA, Heldt D, et al. Biochemical and Structural Insights into Bacterial Organelle Form and Biogenesis. J Biol Chem. 2008 May 23;283(21):14366–75.

20. Havemann GD, Bobik TA. Protein Content of Polyhedral Organelles Involved in Coenzyme B12-Dependent Degradation of 1,2-Propanediol in Salmonella enterica Serovar Typhimurium LT2. J Bacteriol. 2003 Sep;185(17):5086–95.

21. Schmid MF, Paredes AM, Khant HA, Soyer F, Aldrich HC, Chiu W, et al. Structure of Halothiobacillus neapolitanus carboxysomes by cryo-electron tomography. J Mol Biol. 2006 Dec 1;364(3):526–35.

22. Choudhary S, Quin MB, Sanders MA, Johnson ET, Schmidt-Dannert C. Engineered protein nano-compartments for targeted enzyme localization. PloS One. 2012;7(3):e33342.

23. Slininger Lee MF, Jakobson CM, Tullman-Ercek D. Evidence for Improved Encapsulated Pathway Behavior in a Bacterial Microcompartment through Shell Protein Engineering. ACS Synth Biol. 2017 Oct 20;6(10):1880–91.

24. Lawrence AD, Frank S, Newnham S, Lee MJ, Brown IR, Xue W-F, et al. Solution Structure of a Bacterial Microcompartment Targeting Peptide and Its Application in the Construction of an Ethanol Bioreactor. ACS Synth Biol. 2014 Jul;3(7):454–65.

25. Lee MJ, Mantell J, Brown IR, Fletcher JM, Verkade P, Pickersgill RW, et al. De novo targeting to the cytoplasmic and luminal side of bacterial microcompartments. Nat Commun. 2018 Aug 24;9(1):1–11.

26. Slininger Lee M, Tullman-Ercek D. Practical considerations for the encapsulation of multi-enzyme cargos within the bacterial microcompartment for metabolic engineering. Curr Opin Syst Biol. 2017 Oct 1;5:16–22.

27. Dueber JE, Wu GC, Malmirchegini GR, Moon TS, Petzold CJ, Ullal AV, et al. Synthetic protein scaffolds provide modular control over metabolic flux. Nat Biotechnol. 2009 Aug;27(8):753–9.

28. Sampson EM, Bobik TA. Microcompartments for B12-Dependent 1,2-Propanediol Degradation Provide Protection from DNA and Cellular Damage by a Reactive Metabolic Intermediate. J Bacteriol. 2008 Apr 15;190(8):2966–71.

29. Jakobson CM, Tullman-Ercek D, Slininger MF, Mangan NM. A systems-level model reveals that 1, 2-Propanediol utilization microcompartments enhance pathway flux through intermediate sequestration. PLoS Comput Biol. 2017;13(5):e1005525.

30. Cheng S, Fan C, Sinha S, Bobik TA. The PduQ Enzyme Is an Alcohol Dehydrogenase Used to Recycle NAD+ Internally within the Pdu Microcompartment of Salmonella enterica. Hensel M, editor. PLoS ONE. 2012 Oct 15;7(10):e47144.

31. Chowdhury C, Chun S, Pang A, Sawaya MR, Sinha S, Yeates TO, et al. Selective molecular transport through the protein shell of a bacterial microcompartment organelle. Proc Natl Acad Sci. 2015 Mar 10;112(10):2990–5.

32. Uddin I, Frank S, Warren MJ, Pickersgill RW. A Generic Self-Assembly Process in Microcompartments and Synthetic Protein Nanotubes. Small. 0(0):1704020.

33. Lee MJ, Mantell J, Hodgson L, Alibhai D, Fletcher JM, Brown IR, et al. Engineered synthetic scaffolds for organizing proteins within the bacterial cytoplasm. Nat Chem Biol. 2017 Dec 11;14(2):142–7.

34. Huber I, Palmer DJ, Ludwig KN, Brown IR, Warren MJ, Frunzke J. Construction of Recombinant Pdu Metabolosome Shells for Small Molecule Production in *Corynebacterium glutamicum*. ACS Synth Biol. 2017 Nov 17;6(11):2145–56.

35. Cheng S, Sinha S, Fan C, Liu Y, Bobik TA. Genetic analysis of the protein shell of the microcompartments involved in coenzyme B12-dependent 1, 2-propanediol degradation by Salmonella. J Bacteriol. 2011;193(6):1385–1392.

36. Pang A, Frank S, Brown I, Warren MJ, Pickersgill RW. Structural Insights into Higher Order Assembly and Function of the Bacterial Microcompartment Protein PduA. J Biol Chem. 2014 Aug 8;289(32):22377–84.

37. Jakobson CM, Kim EY, Slininger MF, Chien A, Tullman-Ercek D. Localization of Proteins to the 1,2-Propanediol Utilization Microcompartment by Non-native Signal Sequences Is Mediated by a Common Hydrophobic Motif. J Biol Chem. 2015 Oct 2;290(40):24519–33.

38. Nichols TM, Kennedy NW, Tullman-Ercek D. Cargo encapsulation in bacterial microcompartments: Methods and analysis. Methods Enzymol. 2019;617:155–86.

39. Sinha S, Bobik TA. The PduM protein is a structural component of the microcompartments involved in coenzyme 3 B12-dependent 1,2-propanediol degradation by Salmonella. 2012;

40. Kim EY, Slininger MF, Tullman-Ercek D. The effects of time, temperature, and pH on the stability of PDU bacterial microcompartments. Protein Sci. 2014 Oct 1;23(10):1434–41.

41. Schneider CA, Rasband WS, Eliceiri KW. NIH Image to ImageJ: 25 years of image analysis. Nat Methods. 2012 Jul;9(7):671–5.

42. Kerfeld CA. Protein Structures Forming the Shell of Primitive Bacterial Organelles. Science. 2005 Aug 5;309(5736):936–8.

43. Tanaka S, Kerfeld CA, Sawaya MR, Cai F, Heinhorst S, Cannon GC, et al. Atomic-Level Models of the Bacterial Carboxysome Shell. Science. 2008 Feb 22;319(5866):1083–6.

44. Cai F, Menon BB, Cannon GC, Curry KJ, Shively JM, Heinhorst S. The Pentameric Vertex Proteins Are Necessary for the Icosahedral Carboxysome Shell to Function as a CO2 Leakage Barrier. PLOS ONE. 2009 Oct 21;4(10):e7521.

45. Bonacci W, Teng PK, Afonso B, Niederholtmeyer H, Grob P, Silver PA, et al. Modularity of a carbon-fixing protein organelle. Proc Natl Acad Sci. 2012 Jan 10;109(2):478–83.

46. Kim EY, Tullman-Ercek D. A rapid flow cytometry assay for the relative quantification of protein encapsulation into bacterial microcompartments. Biotechnol J. 2014 Mar 1;9(3):348–54.

47. Lassila JK, Bernstein SL, Kinney JN, Axen SD, Kerfeld CA. Assembly of Robust Bacterial Microcompartment Shells Using Building Blocks from an Organelle of Unknown Function. J Mol Biol. 2014 May;426(11):2217–28.

48. Chowdhury C, Chun S, Sawaya MR, Yeates TO, Bobik TA. The function of the PduJ microcompartment shell protein is determined by the genomic position of its encoding gene. Mol Microbiol. 2016 Sep;101(5):770–83.

49. Quin MB, Perdue SA, Hsu S-Y, Schmidt-Dannert C. Encapsulation of multiple cargo proteins within recombinant Eut nanocompartments. Appl Microbiol Biotechnol. 2016 Nov;100(21):9187–200.

50. Lehman BP, Chowdhury C, Bobik TA. The N Terminus of the PduB Protein Binds the Protein Shell of the Pdu Microcompartment to Its Enzymatic Core. Metcalf WW, editor. J Bacteriol. 2017 Apr 15;199(8):e00785-16.

51. Hagen AR, Plegaria JS, Sloan N, Ferlez B, Aussignargues C, Burton R, et al. In Vitro Assembly of Diverse Bacterial Microcompartment Shell Architectures. Nano Lett. 2018 Nov 14;18(11):7030–7.

52. Hagen A, Sutter M, Sloan N, Kerfeld CA. Programmed loading and rapid purification of engineered bacterial microcompartment shells. Nat Commun. 2018 Jul 23;9(1):1–10.

53. Havemann GD, Sampson EM, Bobik TA. PduA is a shell protein of polyhedral organelles involved in coenzyme B-12-dependent degradation of 1,2-propanediol in Salmonella enterica serovar typhimurium LT2. J Bacteriol. 2002 Mar;184(5):1253–61.

54. Pitts AC, Tuck LR, Faulds-Pain A, Lewis RJ, Marles-Wright J. Structural Insight into the Clostridium difficile Ethanolamine Utilisation Microcompartment. Driscoll PC, editor. PLoS ONE. 2012 Oct 29;7(10):e48360.

55. Cai F, Sutter M, Bernstein SL, Kinney JN, Kerfeld C a. Engineering Bacterial Microcompartment Shells: Chimeric Shell Proteins and Chimeric Carboxysome Shells. ACS Synth Biol. 2014 Aug;4(4):444–53.

56. Sutter M, Greber B, Aussignargues C, Kerfeld CA. Assembly principles and structure of a 6.5-MDa bacterial microcompartment shell. Science. 2017 Jun 23;356(6344):1293–7.

57. Cheng S, Liu Y, Crowley CS, Yeates TO, Bobik TA. Bacterial microcompartments: their properties and paradoxes. BioEssays. 2008 Nov;30(11–12):1084–95.

Supporting information

S1 Table. Reported sizes of MCPs. The reported size range for MCPs, the work in which the size was reported, the system being analyzed (Propanediol utilization (Pdu), Ethanolamine utilization (Eut), Carboxysome (Carb)), and the technique used for the analysis (TEM of ultra-thin sections (TEM UTS), TEM of purified MCPs (TEM Pur)).

S1 Fig. Coomassie-stained gel of three biological replicates used for EM images. Lanes: (i) molecular weight standard, (ii-iv) replicates of purified Pdu MCPs.

S2. Fig. Comparison of average diameters measured via NTA and DLS. Error bars represent the standard deviation.

S3 Fig. Full Nanosight/NTA analysis report used in this study.

S4 Fig. DLS analysis of MCPs at 50 µg/mL and 500 µg/mL. Raw correlation data (A), calculated Zave (B), and polydispersity indices (PDI) (C) of MCPs. Intensity (D), number (E), volume (F) particle size distributions of MCPs.

S1 File. Raw sizing data from images.

S2 File. Raw sizing data from Zeta Sizer.

S3 File. Raw sizing data from Nanosight.

S4 File. Raw, uncropped SDS-PAGE gels of purified MCP samples.

Figure 1

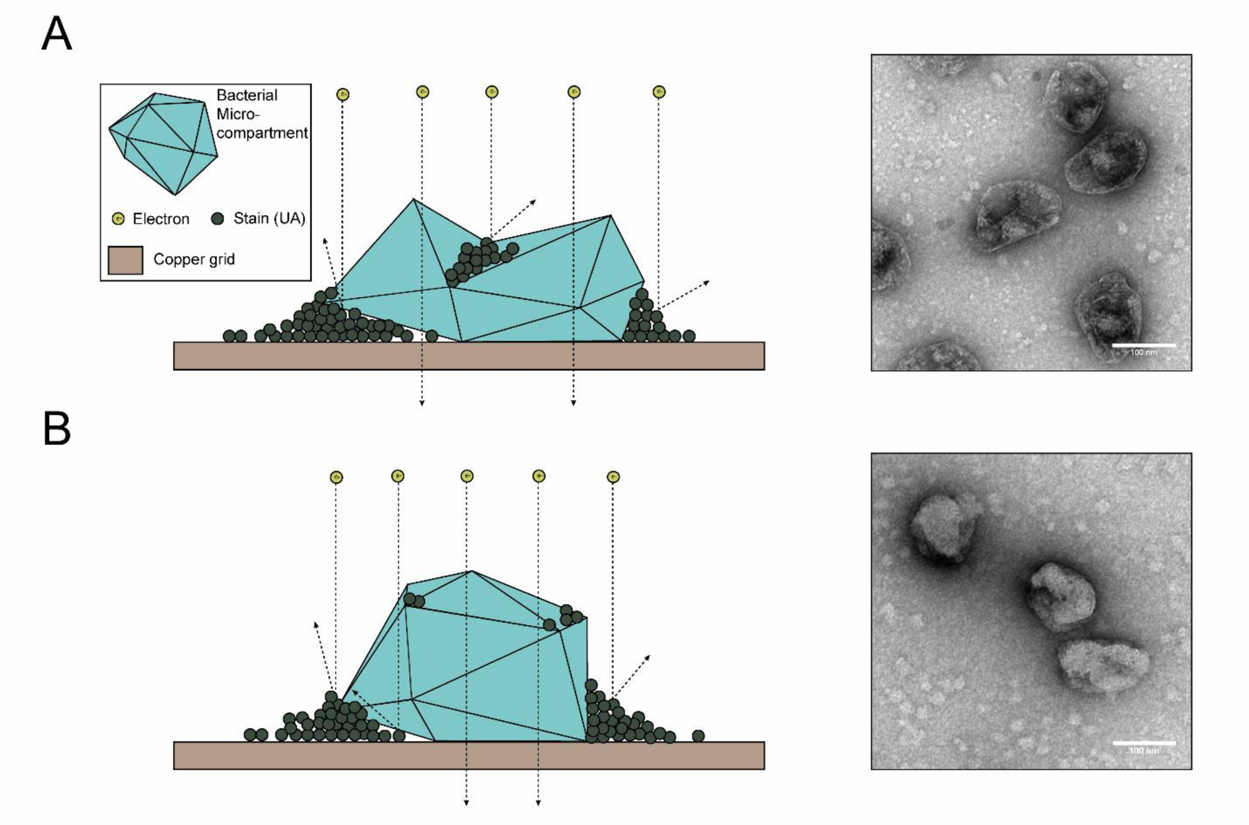
A
Bacterial Micro-compartment
Electron
Stain (UA)
Copper grid
100 nm
B
100 nm

Figure 2

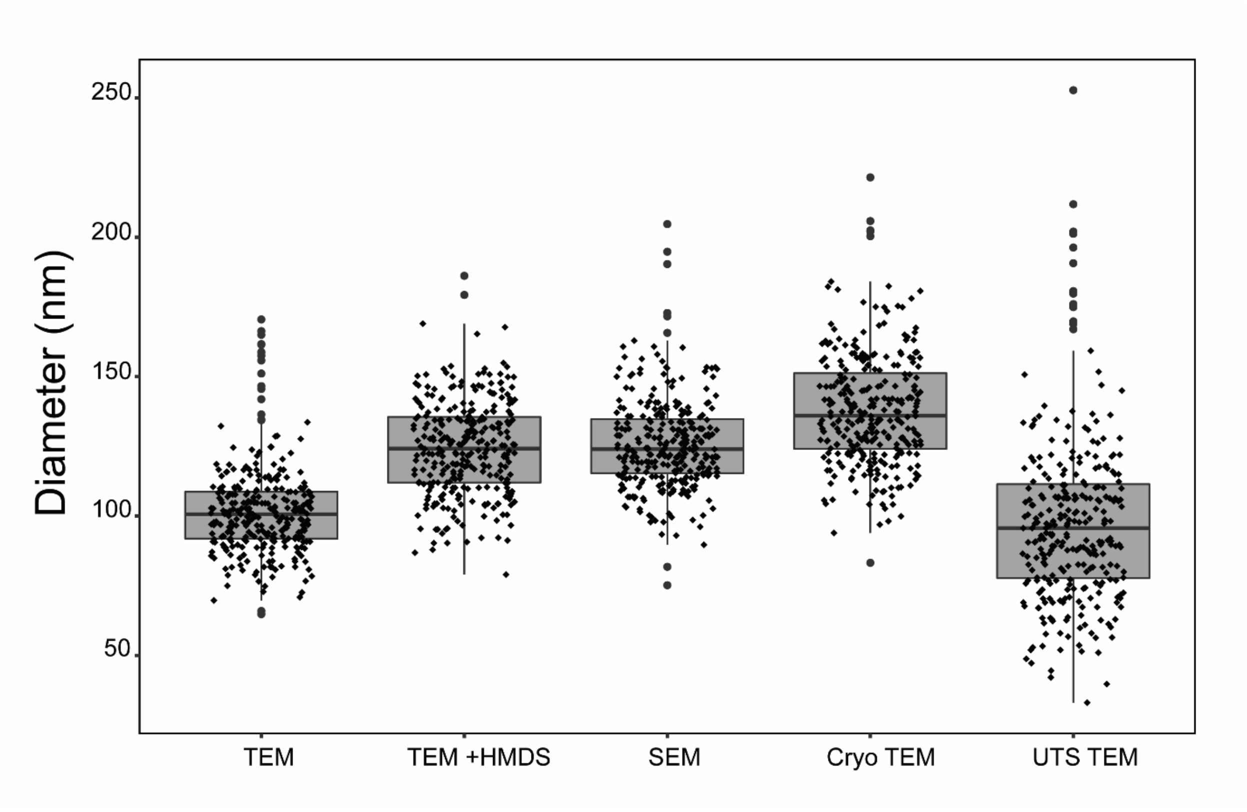
Diameter (nm)
250
200
150
100
50
TEM
TEM +HMDS
SEM
Cryo TEM
UTS TEM

Figure 3

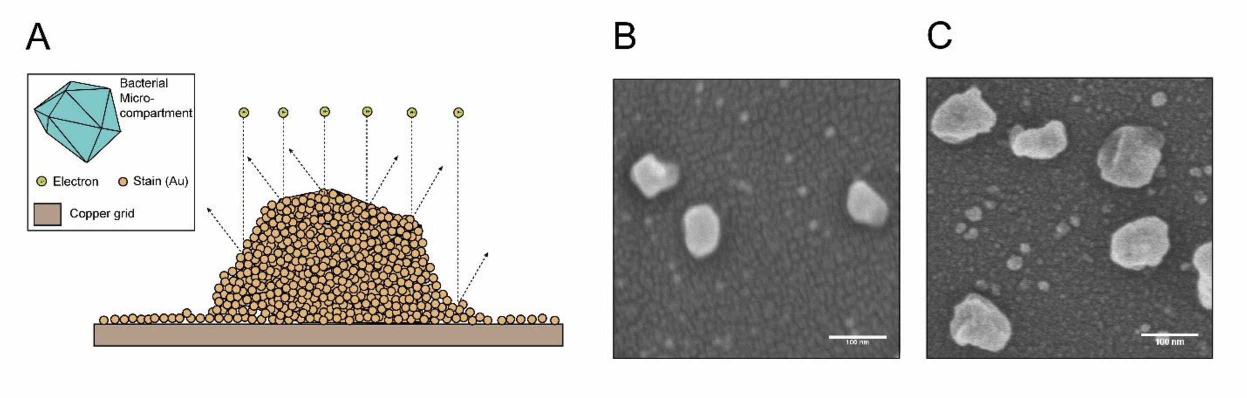
A
Bacterial Micro-compartment
Electron
Stain (Au)
Copper grid
B
100 nm
C
100 nm

Figure 4

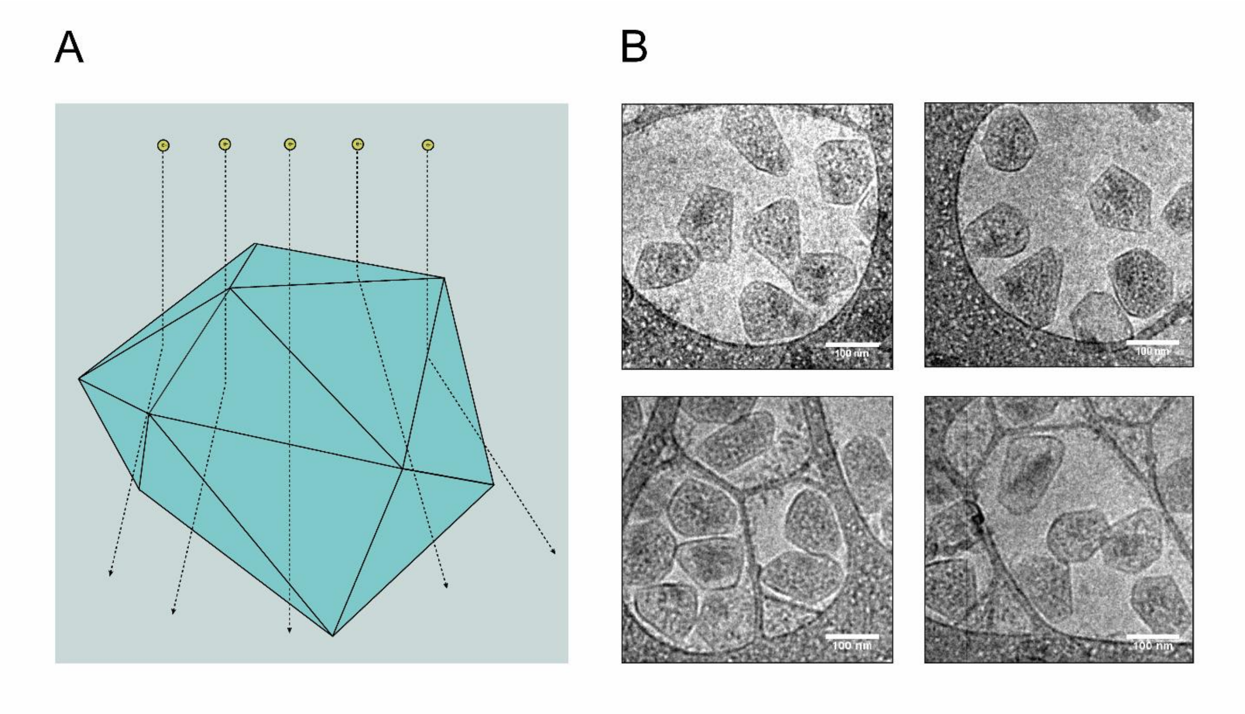
A
B
100 nm
100 nm
100 nm
100 nm

Figure 5

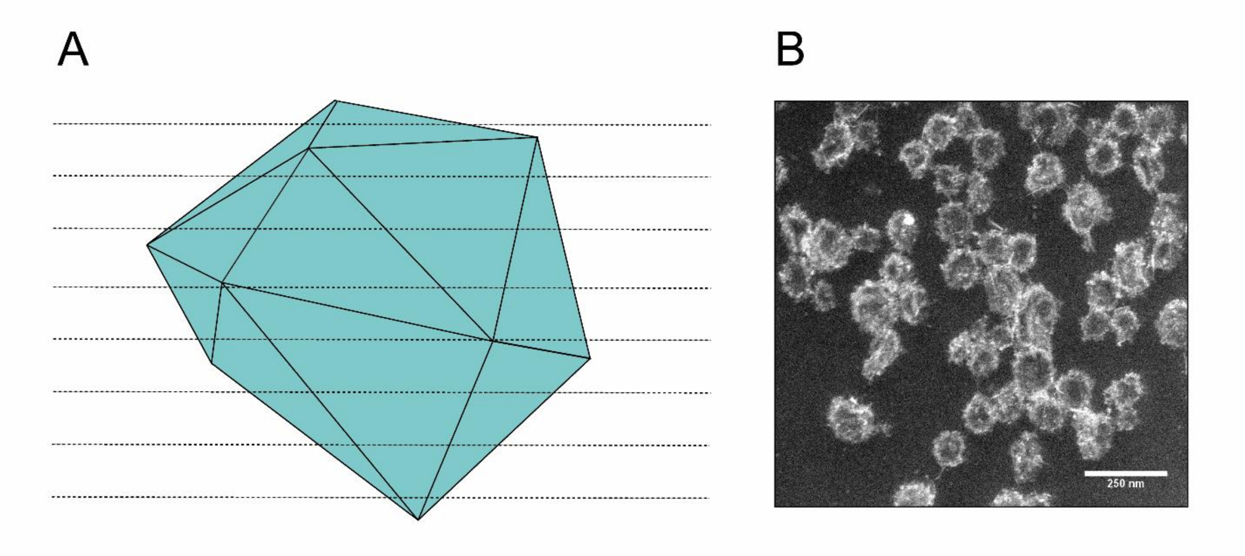

Figure 6

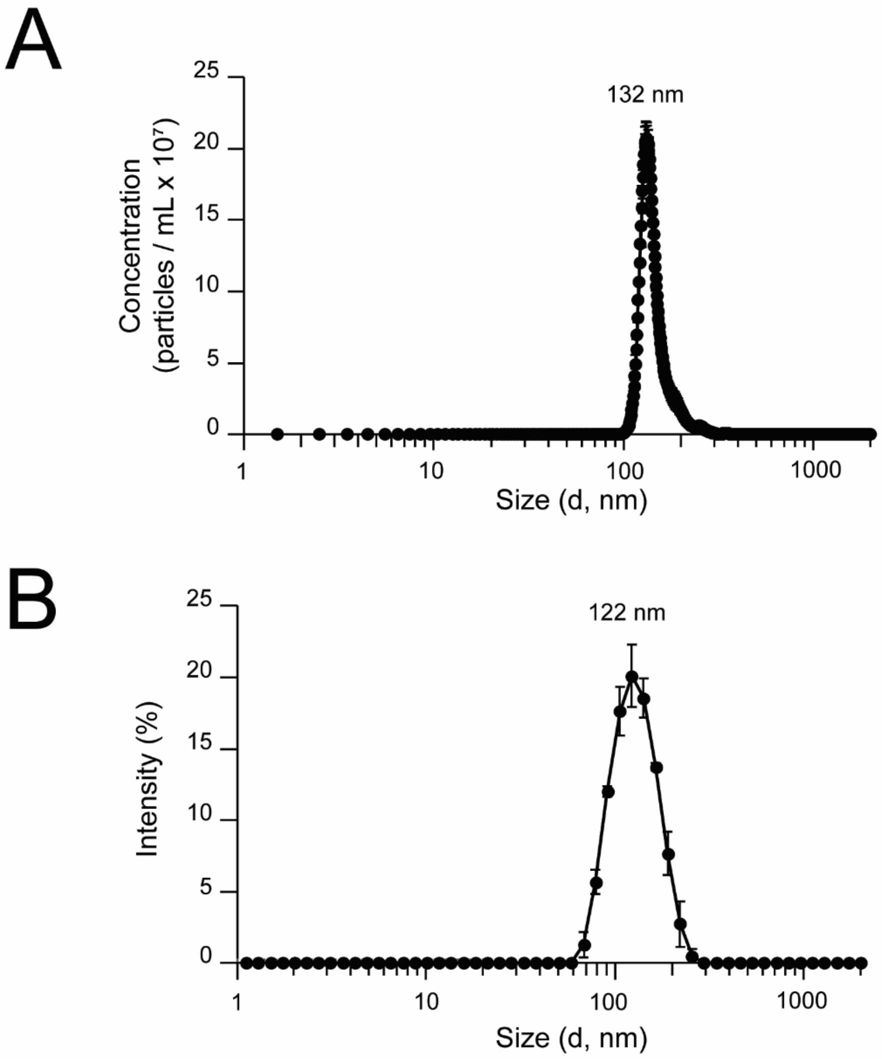
A
25
20
15
10
5
0
132 nm
Concentration (particles / mL x 10⁷)
1
10
100
1000
Size (d, nm)
B
25
20
15
10
5
0
122 nm
Intensity (%)
1
10
100
1000
Size (d, nm)

S1 Figure

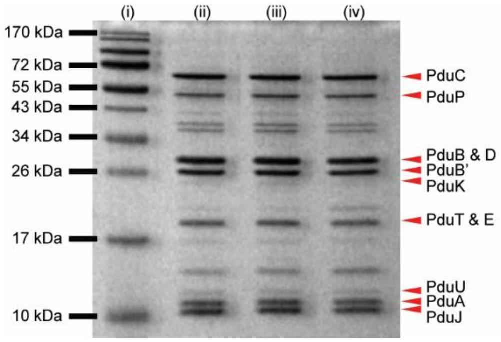
(i)
(ii)
(iii)
(iv)
170 kDa
72 kDa
55 kDa
43 kDa
34 kDa
26 kDa
17 kDa
10 kDa
PduC
PduP
PduB & D
PduB'
PduK
PduT & E
PduU
PduA
PduJ

S1 Table

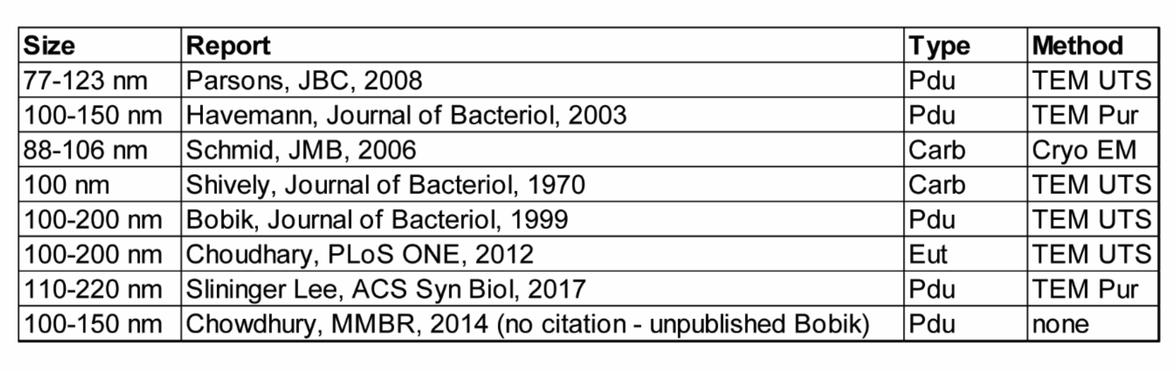

Size	Report	Type	Method
77-123 nm	Parsons, JBC, 2008	Pdu	TEM UTS
100-150 nm	Havemann, Journal of Bacteriol, 2003	Pdu	TEM Pur
88-106 nm	Schmid, JMB, 2006	Carb	Cryo EM
100 nm	Shively, Journal of Bacteriol, 1970	Carb	TEM UTS
100-200 nm	Bobik, Journal of Bacteriol, 1999	Pdu	TEM UTS
100-200 nm	Choudhary, PLoS ONE, 2012	Eut	TEM UTS
110-220 nm	Slininger Lee, ACS Syn Biol, 2017	Pdu	TEM Pur
100-150 nm	Chowdhury, MMBR, 2014 (no citation - unpublished Bobik)	Pdu	none

S2 Figure

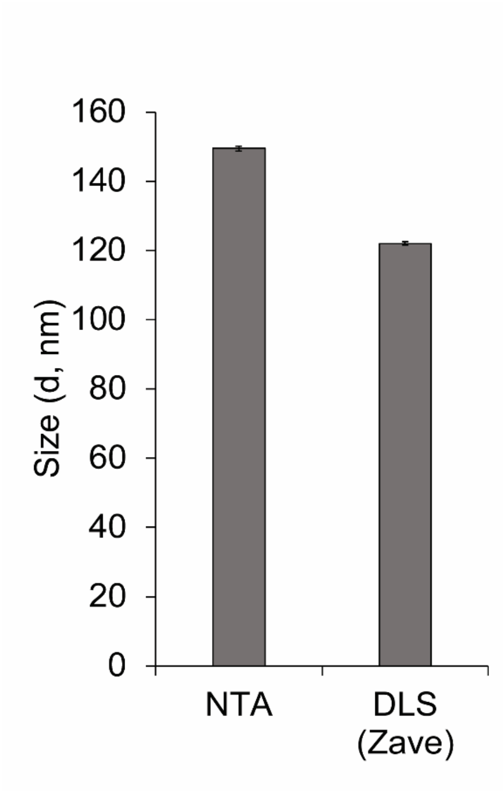

S3 Figure

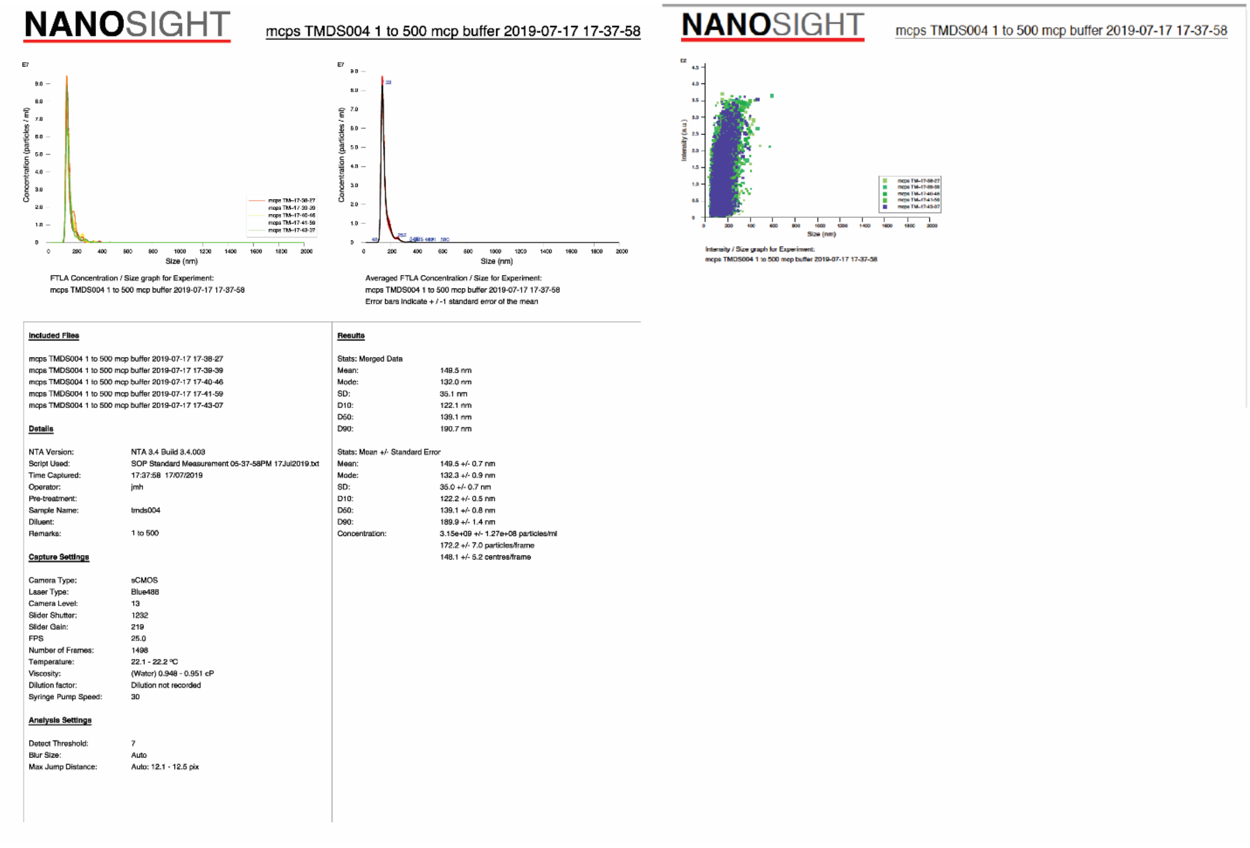

mcps TMDS004 1 to 500 mcp buffer 2019-07-17 17-37-58

FTLA Concentration / Size graph for Experiment:
mcps TMDS004 1 to 500 mcp buffer 2019-07-17 17-37-58

Averaged FTLA Concentration / Size for Experiment:
mcps TMDS004 1 to 500 mcp buffer 2019-07-17 17-37-58
Error bars indicate + / -1 standard error of the mean

Included Files

mcps TMDS004 1 to 500 mcp buffer 2019-07-17 17-38-27
mcps TMDS004 1 to 500 mcp buffer 2019-07-17 17-39-39
mcps TMDS004 1 to 500 mcp buffer 2019-07-17 17-40-46
mcps TMDS004 1 to 500 mcp buffer 2019-07-17 17-41-59
mcps TMDS004 1 to 500 mcp buffer 2019-07-17 17-43-07

Details

NTA Version:	NTA 3.4 Build 3.4.003
Script Used:	SOP Standard Measurement 05-37-58PM 17Jul2019.txt
Time Captured:	17:37:58 17/07/2019
Operator:	jmh
Pre-treatment:	
Sample Name:	tmds004
Diluent:	
Remarks:	1 to 500

Capture Settings

Camera Type:	sCMOS
Laser Type:	Blue488
Camera Level:	13
Slider Shutter:	1232
Slider Gain:	219
FPS	25.0
Number of Frames:	1498
Temperature:	22.1 - 22.2 °C
Viscosity:	(Water) 0.948 - 0.951 cP
Dilution factor:	Dilution not recorded
Syringe Pump Speed:	30

Analysis Settings

Detect Threshold:	7
Blur Size:	Auto
Max Jump Distance:	Auto: 12.1 - 12.5 pix

Results

Stats: Merged Data

Mean:	149.5 nm
Mode:	132.0 nm
SD:	35.1 nm
D10:	122.1 nm
D50:	139.1 nm
D90:	190.7 nm

Stats: Mean +/- Standard Error

Mean:	149.5 +/- 0.7 nm
Mode:	132.3 +/- 0.9 nm
SD:	35.0 +/- 0.7 nm
D10:	122.2 +/- 0.5 nm
D50:	139.1 +/- 0.8 nm
D90:	189.9 +/- 1.4 nm
Concentration:	3.15e+09 +/- 1.27e+08 particles/ml
	172.2 +/- 7.0 particles/frame
	148.1 +/- 5.2 centres/frame

mcps TMDS004 1 to 500 mcp buffer 2019-07-17 17-37-58

Intensity / Size graph for Experiment:
mcps TMDS004 1 to 500 mcp buffer 2019-07-17 17-37-58

S4 Figure

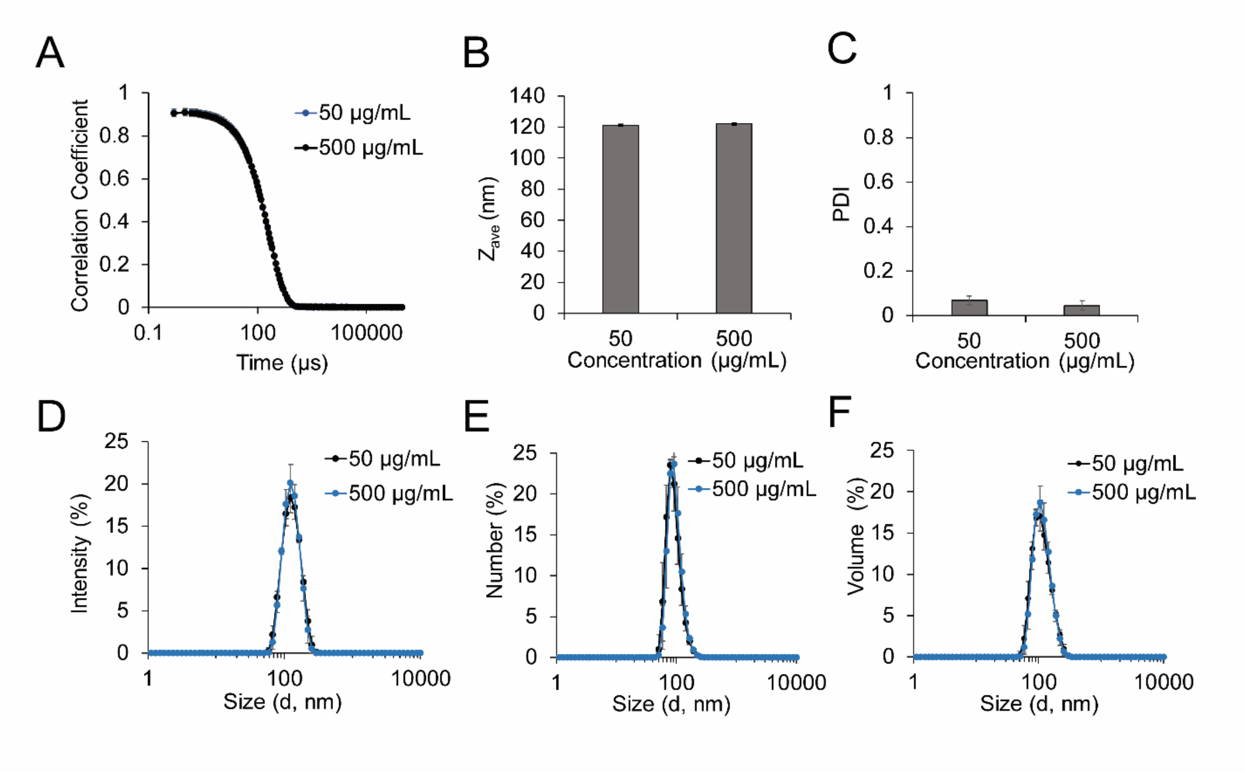
A
Correlation Coefficient
1
0.8
0.6
0.4
0.2
0
0.1
100
100000
Time (μs)
50 μg/mL
500 μg/mL
B
Z_{ave} (nm)
140
120
100
80
60
40
20
0
50
500
Concentration (μg/mL)
C
PDI
1
0.8
0.6
0.4
0.2
0
50
500
Concentration (μg/mL)
D
Intensity (%)
25
20
15
10
5
0
1
100
10000
Size (d, nm)
50 μg/mL
500 μg/mL
E
Number (%)
25
20
15
10
5
0
1
100
10000
Size (d, nm)
50 μg/mL
500 μg/mL
F
Volume (%)
25
20
15
10
5
0
1
100
10000
Size (d, nm)
50 μg/mL
500 μg/mL